

Cite this: *J. Mater. Chem. A*, 2017, 5, 24159

Tailoring the chemistry of blend copolymers boosting the electrochemical performance of Si-based anodes for lithium ion batteries†

Elhadi N. Attia,  ‡ Fathy M. Hassan,  ‡ Matthew Li, Rasim Batmaz, Ali Elkamel and Zhongwei Chen  *

Flexible and conductive carbon networks have been widely employed to overcome the stability degradation of highly sought-after Si-based anodes for Li-ion batteries (LIBs). However, little attention has been paid to the contact intimacy of such a network. In this contribution, we designed a polymer blend of polyvinylpyrrolidone (PVP) and polyacrylonitrile (PAN) which was self-assembled onto the surface of silicon nanoparticles (SiNPs) allowing for the generation of a very intimate coating of a silicon dioxide and nitrogen-rich carbon shell upon sluggish heat treatment. This methodology capitalizes on the surface interaction of PVP with SiNPs to provide a sturdy nanoarchitecture. The addition of PVP improves the stability and adhesion of PAN to the carbon-based matrix which surrounds the silicon particles leading to enhanced stability. In addition to being a very scalable fabrication process, our novel blend of PVP and PAN allowed for an electrode with high reversibility. When compared with a standard electrode Si/PVDF framework, this material demonstrated a significantly superior 1st discharge capacity of 2736 mA h g⁻¹, high coulombic efficiency, and excellent cycling stability for 600 cycles at a high rate of 3 A g⁻¹.

Received 21st September 2017
Accepted 26th October 2017

DOI: 10.1039/c7ta08369f

rsc.li/materials-a

Introduction

In recent years, the intensification of climate change has led to an increasing level of interest in the improvement of green-renewable energy systems to replace fossil fuels.¹ Energy storage devices used to buffer the intermittent nature of solar and wind energy have become one of the key limiting factors. Compared with other energy storage technologies, rechargeable Li-ion batteries are commonly implemented in different applications such as mobile devices, electric vehicles (EVs), hybrid electric vehicles (HEVs), and medical microelectronic devices due to their high specific and volumetric energy densities as well as their lower production costs.^{1–8} However, current LIBs are reaching their theoretical limits and can no longer be further improved/optimized, prompting researchers to look for next-generation technologies. Fabrication of such a battery technology with low-cost electrode materials and high-energy density can lead to significant improvements in the performance and lifetimes of products that use LIBs, effectively combating against climate change.^{9–11}

Department of Chemical Engineering, Waterloo Institute for Nanotechnology, Waterloo Institute for Sustainable Energy, University of Waterloo, 200 University Ave. W., Waterloo, Ontario, Canada, N2L 3G1. E-mail: zhwen@uwaterloo.ca

† Electronic supplementary information (ESI) available. See DOI: 10.1039/c7ta08369f

‡ These authors contributed equally.

Among the many candidates for anode materials for high-energy density LIBs, silicon (Si) has shown great promise as a next generation negative electrode for LIBs due to its natural abundance, relatively low working potential (0.5 V vs. Li/Li⁺), low toxicity, safety, and environmental friendliness. Moreover, compared to the graphite anode materials of commercial LIBs, Si has a high theoretical specific capacity reaching 4200 mA h g⁻¹ (Li_{4.4}Si) when fully lithiated representing a ten-fold increase in potential capacity.^{9,12–14} For these reasons, many researchers have been intensively studying Si as an anode material in the last few years. However, Si experiences an excessive volume expansion (>300%) which leads to poor cycling stability, rapid capacity loss and overall degradation of electrochemical performance due to the severe cracks and fast pulverization of the active material.^{12,14–19} Additionally, the continuous volume expansion (lithiation) and contraction (delithiation) result in the detrimental continuous formation of a solid electrolyte interphase (SEI) layer on the Si particle surface by a side reaction between the electrolyte and exposed lithiated Si. This phenomenon leads to an unstable SEI, short cycle life, and large irreversible capacities during cycling.^{18–21} In addition, Si suffers from low electrical conductivity compared to graphite, and the diffusion coefficient of Li in Si is low ($\sim 10^{-13}$ cm² s⁻¹).²²

Recent work in the development of a Si anode for LIBs has focused on the incorporation of a flexible/breathable conductive support for Si particles of some form with varying degrees of

success.²³ However, the lack of an intimate contact between the conductive support and Si particles limits the potential of such a concept. Moreover, complicated synthesis techniques significantly reduce any commercial viability of such concepts. In this work, we implement the extremely scalable sluggish heat treatment (SHT)²⁴ on an electrode composed of a rational blend of commercially available polymers: PVP and PAN in addition to SiNPs. The interaction between PVP and the hydroxy groups of Si allows for extremely intimate contact between the conductive support and SiNPs, as well as, the formation of a thin layer of SiO₂ over the surface of SiNPs. In combination with the large PAN derived N-rich graphene sheets this electrode was able to deliver high capacity with excellent coulombic efficiency and cycling stability.

Experimental section

Fabrication of composite electrodes

SiNPs with an average diameter of 50 to 60 nm were bought from Nanostructured & Amorphous Materials, Inc. (Houston, TX), and we fabricated the electrodes for LIB testing. Typically, about 20% of PVP ($M_w = \sim 1300\ 000$, Sigma-Aldrich Co) was used as a binder, which was dissolved in deionized distilled water (DDI) at room temperature for about 20 minutes. Then, 80% of SiNPs were added to the PVP solution and mixed by stirring and ultrasonication for about 90 minutes to achieve a homogeneous dispersion and freeze-dried. For working electrodes, the slurry contained 78% of Si/PVP composite, 20% of PAN solution ($M_w = 150.000$, Sigma-Aldrich Co, dissolved in DMF at 5 wt% PAN) and 2% of graphene oxide (GO) that was used as an oxidizing agent. GO was synthesized by a modified Hummer's method.²⁵ The mixture was mixed under magnetic stirring and ultrasonication at room temperature for 30 minutes to achieve a homogeneous slurry of the electrode components. The slurry was coated on a copper foil current

collector by doctor-blading and dried in a convection oven at 80 °C for 1 hour, followed by drying in a vacuum oven at 85 °C overnight. Electrodes were cut into circular discs of 1.2 cm diameter and the Si mass loading was typically 0.2–1.3 mg cm⁻². The electrodes were exposed to the SHT process using a quartz tube at two different temperatures, 450 or 750 °C, by slowly heating in an argon atmosphere and holding for 10 minutes, followed by cooling (Fig. 1). This treatment technique could create coherent shells that stabilized the SEI and improved the conductivity of the electrode materials by partially carbonizing the PAN binder leading to a flexible shell providing flexibility and porosity.²⁴ The optical images of the electrode before and after SHT with a change in the electrode color from brown to black are shown in ESI Fig. S1.† Coin-type half cells (2032 type) with lithium foil (Aldrich, USA) used as a counter electrode were fabricated in an Ar-filled glove box (MBRAUN 10, USA) in an argon atmosphere with water and oxygen content both under 0.5 ppm. The electrolyte was composed of LiPF₆ (1 M) in 30 wt% ethylene carbonate (EC), 60 wt% dimethyl carbonate (DMC), and 10 wt% fluorinated ethylene carbonate (FEC). A polypropylene separator was used to separate the positive and negative electrodes. Each coin cell contained ~40 μl of the electrolyte.

Materials characterization

The morphological features of the electrode materials were imaged using transmission electron microscopy (JEOL 2010F TEM/STEM field emission microscope, located at the Canadian Center for Electron Microscopy (CCEM) at McMaster University, Hamilton, Ontario-Canada). The samples were prepared by gently scratching some materials from the surface electrode coating and then dispersing the materials in pure methanol and drop-casting onto the TEM grid. A scanning electron microscope (ZEISS ULTRA PLUS SEM) was used to investigate the morphology of the electrode materials. X-ray photoelectron

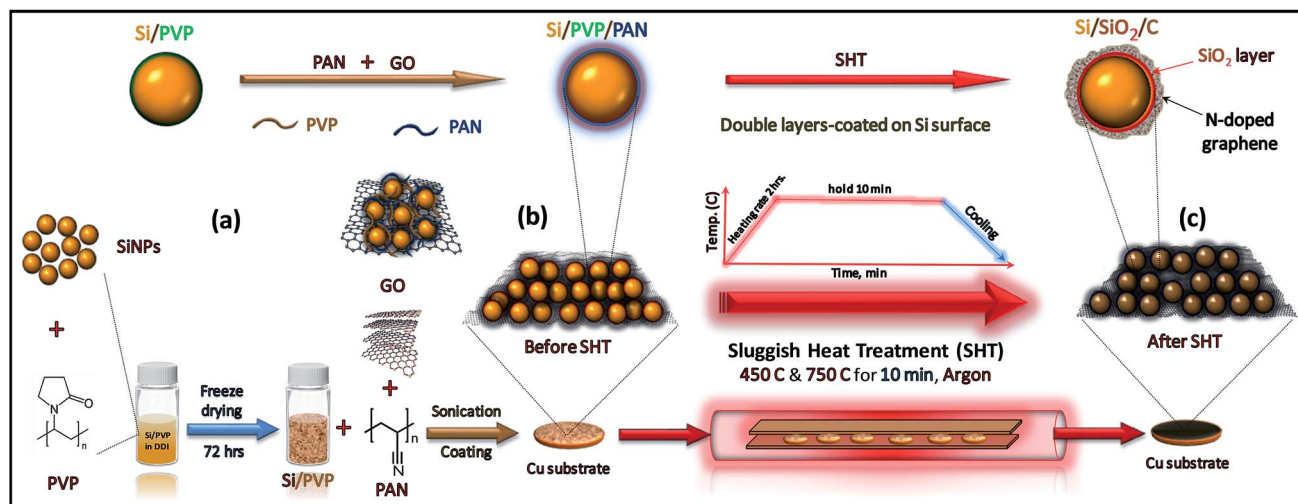


Fig. 1 Schematic showing the fabrication procedure of the electrode and SHT process. Copolymer blend shielding each SiNP and creating a breathable shell; (a) synthesis of the electrode from SiNPs, PVP, PAN, and GO before coating on the Cu foil, (b) electrode before SHT, and (c) electrode after SHT.

spectroscopy (XPS) using a PHI Quantera XPS spectrometer located at the Ontario Center for Characterization of Advanced Materials at University of Toronto was conducted to analyze the chemical composition of the electrode materials. Raman scattering spectra were recorded on a Bruker Senterra system (532 nm laser). Thermogravimetric analysis (TGA) was completed using a TGA Q500 under air in a temperature range of 30 to 800 °C and at a ramp rate of 10 °C min⁻¹. Differential scanning calorimetry (DSC) analysis was performed with an American TA SDT Q600 at a heating rate of 10 °C min⁻¹ under a nitrogen atmosphere and in the temperature range of 30 to 400 °C.

Results and discussion

Electrode fabrication and design are schematically shown in Fig. 1. To achieve an intimate contact between the carbon shell

and the SiNPs, it is crucial to ensure the intimate mixing and coverage of the carbon precursor with the SiNPs. Although PAN has been shown to be easily converted into a highly conductive graphene-like conductive support, the relatively lower dielectric constant of its solvent (*N,N*-dimethylformamide, DMF) and subsequently its thin electrical double layer cannot achieve the same SiNP suspension homogeneity when compared to water. By dispersing the SiNPs in water with PVP, an extremely stable suspension is obtained with PVP self-assembled into an intimate shell around the Si particles, interacting with the Si's natural hydroxy groups. After freeze drying and homogenizing with a PAN solution in DMF and a small portion of GO, the slurry was cast onto a copper foil and dried. Then, the electrodes were inserted into the smaller tube and heated by thermal treatment (SHT)²⁴ at temperatures of 450 °C and 750 °C (Fig. 1). The SHT induces a chemical modification in the intimately

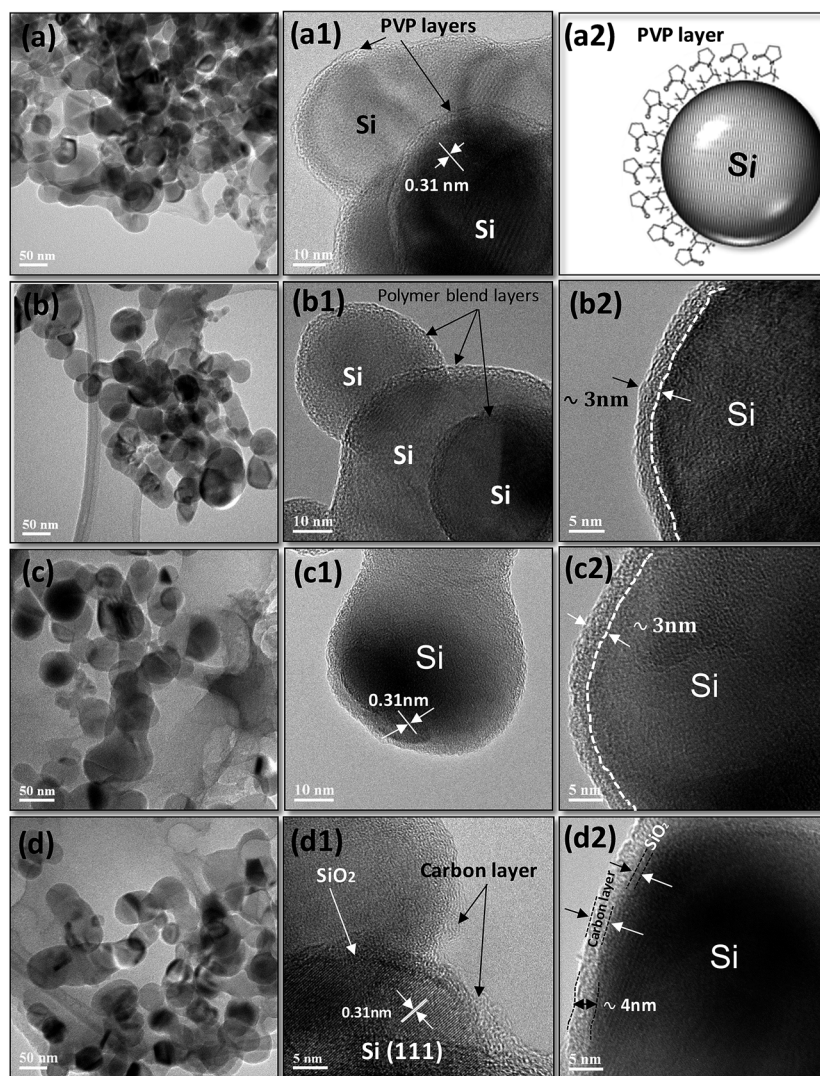


Fig. 2 (a) HAADF-STEM image of a few Si particles intimately wrapped by PVP, (a1) HRTEM image of a few Si particles coated by PVP, (a2) schematic of the PVP coated Si particle, (b–b2) TEM images of the Si/PVP/PAN electrode before SHT with different magnifications, (c–c2) TEM images of the Si/PVP/PAN electrode treated at 450 °C, and (d–d2) TEM images of the Si/PVP/PAN electrode treated at 750 °C with different magnifications from low to high.

wrapped PVP/PAN polymer blend and transforms it into coherent, flexible and conductive shells nesting the SiNP inside.

The morphology of the electrode materials at different stages was analyzed by HRTEM. Fig. 2(a and a1) reveal a thin layer over the Si particles, indicating that our envisioned intimate wrapping of PVP over Si particles was successful after freeze drying as schematically shown in Fig. 2(a2). In addition, SEM images show the morphology of Si/PVP after freeze drying which reveals that Si particles are embedded in the matrix of the PVP polymer, and self-assembled in a leaf-like morphology (Fig. S2†). After mixing with PAN, the composite (Fig. 2(b–b2)) shows little change in the morphology. However, upon closer investigation, it was found that the new composite possesses a thicker shell of ~ 3 nm (Fig. 2(b2)) indicating the proper assembly of PAN over PVP/SiNP. The TEM images of the electrode after SHT at 450°C are shown in Fig. 2(c–c2) and the TEM images of the electrode after being treated at 750°C are shown in Fig. 2(d–d2). Surprisingly, little morphological difference is found between the electrodes with or without heat treatment indicating that the as-designed structure is maintained after heat treatment at both 450°C and 750°C . Moreover, a thicker coating (~ 4 nm) as shown in Fig. 2(d2) was found on the surface of all SiNPs after

heat treatment at 750°C when compared to the only ~ 3 nm coating of the 450°C sample which we believe is a result of more SiO_2 . The high magnification TEM confirms that the lattice fringe spacing of 0.31 nm corresponded to the (111) Si planes after SHT at 750°C as shown in Fig. 2(d1).

Energy dispersive spectroscopy (EDS) elemental mapping was performed on the electrodes under all conditions. Fig. 3(a–a3) reveal that, without heat treatment, the carbon and oxygen distribution is not well defined with respect to the Si mapping for the area marked in Fig. 3a. However, when the sample is treated at 450°C (Fig. 3(b)) and 750°C (Fig. 3(c)), the distribution of both carbon (Fig. 3(b2) and (c2)) and oxygen (Fig. 3(b3) and (c3)) appears to be abundant in places where there is no Si (Fig. 3(b1) and (c1)). Furthermore, when the 750°C heat treated sample is mapped with electron energy loss spectroscopy (EELS), a very clear concentration of both carbon (Fig. 3(d2)) and oxygen (Fig. 3(d3)) signals can be found at the edge of the Si particles for the area marked in Fig. 3c. This indicates that Si particles have a double coating of amorphous carbon and possibly an oxygen rich, thin Si film. Moreover, X-ray photoelectron spectroscopy (XPS) of Si 2p (Fig. 3e) reveals that the Si in the sample treated at 750°C is significantly more oxidized

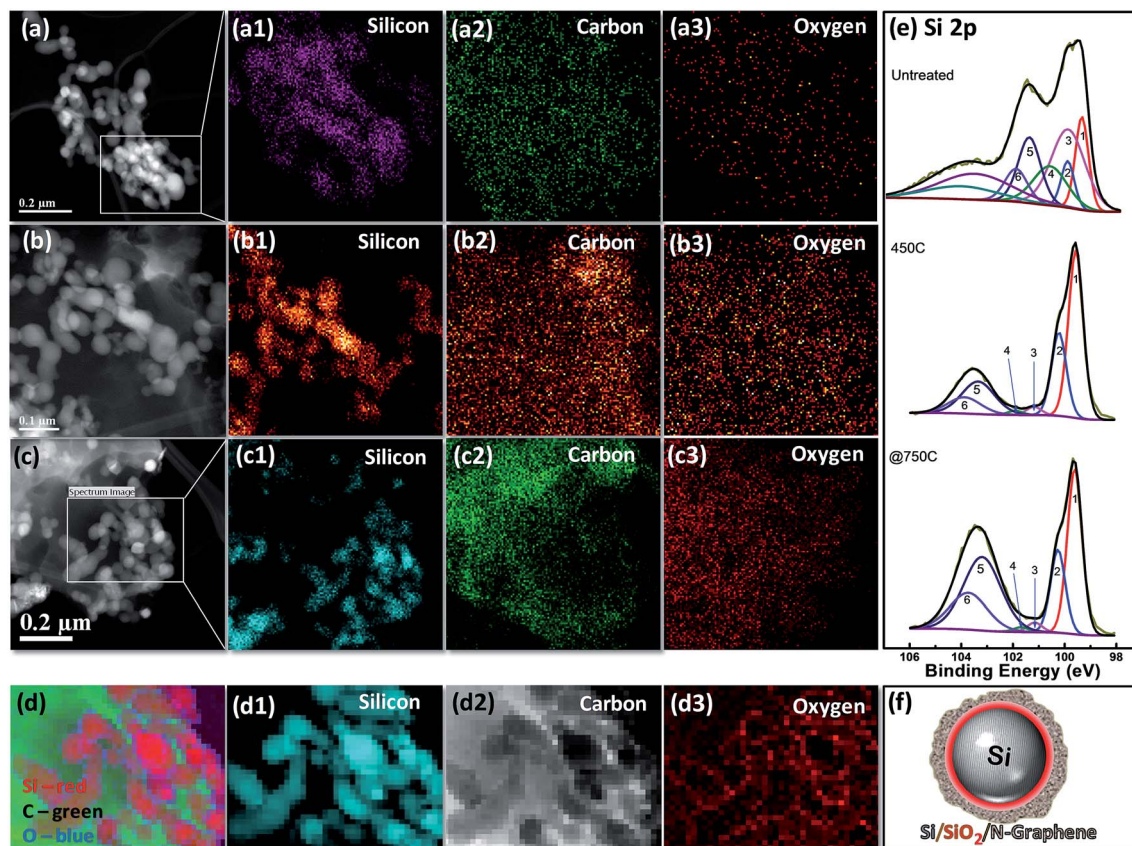


Fig. 3 (a) Higher magnification HAADF-STEM image of a few Si particles before SHT, (a1–a3) corresponding elemental mapping of Si, C and O of the area selected in the image (a), (b) HAADF-STEM image of the electrode surface treated at 450°C , (b1–b3) corresponding EDS mapping of Si, C, and O of the image (b), (c) HAADF-STEM image of Si particles treated at 750°C , (c1–c3) corresponding EDS mapping of Si, C, and O of the area marked in the image (c), (d) EELS elemental mapping of Si (red), C (green), and O (blue), (d1–d3) elemental mapping by EELS for the area selected in the image (c), (e) high-resolution XPS of Si 2p spectra of the electrode materials before and after SHT, and (f) a schematic showing the core Si particle with the surrounding layers of SiO_2 and N-doped graphene.

with a stronger peak at the higher binding energy levels compared to the untreated and 450 °C heat treated sample. The combination of a carbon and a SiO₂ shell around the Si particles as illustrated in Fig. 3f will mitigate the negative effects of Si pulverization during cycling leading to improved cycling stability.²⁶

The role of the addition of PVP was investigated by the thermogravimetric analysis (TGA) plots shown in Fig. 4a. Samples with and without PVP were analyzed with a TGA program that emulated the electrode treatment conditions that we applied, where the samples were ramped to either 450 °C or 750 °C and held at these temperatures for 1 hour. At 450 °C, no increase in mass is observed, whereas at a heat treatment temperature of 750 °C, a mass increase is clearly present. The mass increases corroborate well our previous speculation of SiO₂ coating around Si from the XPS and TEM results and suggest that the formation of significant amounts of SiO₂ did indeed occur. More importantly, without PVP, the increase in mass occurs at a higher temperature (~750 °C) and with a significantly lower magnitude of increase compared to the sample with PVP. This analysis clearly demonstrates that PVP is able to act as an oxidizing agent for Si and accelerate the partial oxidation process of Si to SiO₂. However, DSC results (Fig. 4b) indicate that PVP has a melting point around 100 °C which is much lower than 450 °C. We theorize that this apparent contradiction can be explained by the residual PVP's oxygen

groups that were not removed at 100 °C and were able to be consumed by Si at around 700 °C. As expected, pure PAN did not have any endothermic peak, but showed a sharp exothermic peak at 300 °C corresponding to the cyclization of PAN nitrile groups by a free radical reaction^{27–30} which was associated with the initial weight loss of pure PAN at the same temperature of TGA of pure PAN in air (Fig. S3†). However, pure PVP did not have any exothermic peak but showed a melting peak at 100 °C (ref. 31) and what appears to be another endothermic peak starting at ~380 °C,²⁸ which corresponds to the TGA weight loss (Fig. S3†). After incorporating PAN into the electrode materials, the DSC results show some changes in endothermic peaks with the samples. Samples with PAN and PVP displayed clear exothermic peaks in the range from 297 to 302 °C due to the free radical cyclization reaction of the nitrile group (C≡N) present in the structure of PAN.^{27,29,30} Interestingly, the endothermic peaks of the samples with both PVP and PAN are delayed to a higher temperature. This is mostly because PVP is miscible with the PAN polymer and a result of hydrogen bonding interactions between the proton acceptor of PVP and α -hydrogens of PAN.^{32,33} This is clearly demonstrated by the carbon layer in TEM images after adding PAN to the electrode materials as shown in Fig. 2(b2) with no phase separation appearing. From the DSC curve, it is clear that the cyclization peak of PVP/PAN is much broader than that of pure PAN which is in alignment with previous studies.³⁴

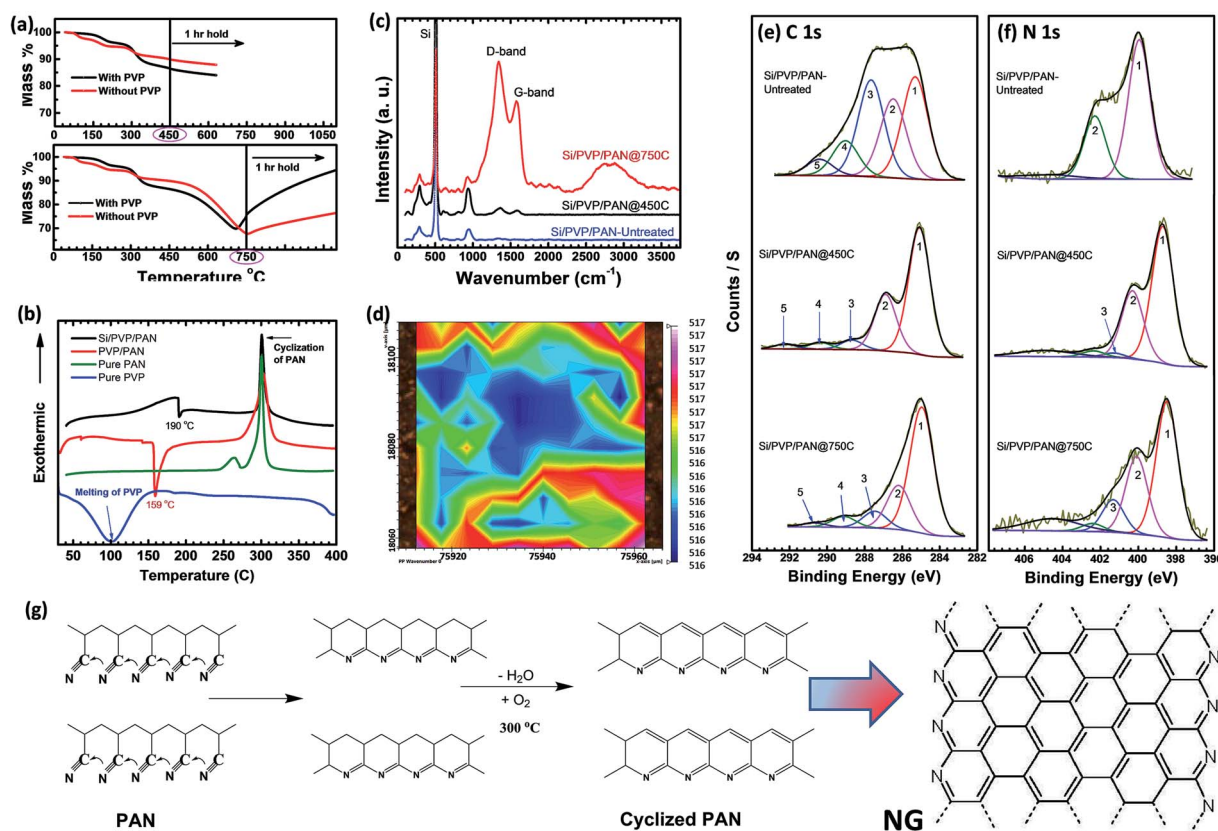


Fig. 4 (a) TGA of the electrode materials with and without PVP in air, (b) DSC analysis of the electrode materials in nitrogen, (c) Raman spectrum of the electrode materials before and after SHT, (d) Raman mapping of the fwhm of the Si peak, high-resolution XPS spectra of the electrode materials before and after SHT: (e) C 1s and (f) N 1s, and (g) schematic of the cyclization mechanism for PAN.

Raman spectroscopy was performed on electrodes before and after SHT to identify the chemical structure of the electrode materials (Fig. 4c). A clear difference between the samples can be recognized. The characteristic carbon peaks appeared at 1342 and 1576 cm^{-1} after SHT, which match well with the 'D' and 'G' bands, respectively, with an I_D/I_G ratio of 0.85. As expected, the D and G band intensities increase with increasing temperature, indicating a higher degree of carbonization. This graphitized carbon is related to the cyclization of PAN during SHT.²⁴ Interestingly, the Si peak was found to be shifted towards a smaller wave number which stems from the surface stresses induced by the formation of a shell of SiO_2 and the carbon materials.^{24,35,36} Two small peaks at 290 and 930 cm^{-1} were also found which we believe are associated with Si–O–Si bonding and Si–OH stretching on the Si surface, respectively.^{24,26,35,37} Raman mapping of the full-width at half maximum of a specific area shows these stresses of the Si peak after SHT in Fig. 4d. Furthermore, the high-resolution XPS binding energy spectra of carbon C 1s (Fig. 4e) reveal a peak (1) located at 285.3 eV (associated with the presence of the sp^3 carbon bond) prior to heat treatment.^{24,38} After SHT at both temperatures, this peak shifted slightly towards a lower binding energy (284.9 eV) which is due to the sp^2 hybridization of PAN into a graphitic type carbon.^{24,38–43} On the other hand, the peak (2) centered at 286.5 eV may be attributed to the carbon atoms bonded to nitrogen in C–N bonds.⁴⁴ With temperature increasing, this peak decreases which reveals a significant transformation of the polymer structure. Peaks (3–5) centered in the range of 287.5 to 289 eV are attributed to oxygenated carbon in the polymer matrix.^{45–49} The high-resolution N 1s spectra (Fig. 4f) were divided into main three components of nitrogen differentiated by their binding energies at 398.7, 400, and 401.3 eV which are associated with the pyridinic-N, pyrrolic-N, and graphitic-N forms of nitrogen, respectively.^{50,51} The relative content of the pyridinic-N and graphitic-N structures likely increased during the heat treatment due to the relative thermal stability of each form. However, the existence of the nitrogen group after high temperature (750 °C) heat treatment allows for nitrogen groups to act as electronegative sites for electrostatically hindering any migration of SiNP during cycling. These results are in good alignment with the cyclization mechanism of PAN and its transformation into a N-rich graphene-like structure (Fig. 4g).

To illustrate charge storage performance, the coin cells that were made with treated electrodes were characterized by cyclic voltammetry (CV) in Fig. 5a. The CV curve of the electrode treated at 750 °C reveals the activation process of the electrode for five cycles within the voltage window of 0.01 V and 1.10 V at a scan rate of 0.05 mV s^{-1} . The CV curve of the first cycle (black line) is apparently dissimilar to the following cycles. Two oxidation peaks are observed at 0.53 and 0.38 V (*versus* Li^+/Li) during charging, which indicates the lithium extraction process in Si.²⁴ During discharge, the peak at 0.2 V starts at the second cycle, which is absent in the first cycle, which suggests the transformation from crystalline Si to amorphous phase Li_xSi .^{8,24} With cycling, all peaks become stronger and sharper, which is a common property for the transition from crystalline Si to amorphous Si due to lithiation/delithiation.^{12,26,52} Both treated

electrodes show almost similar CV profiles with stronger peaks for the electrode treated at 450 °C as shown in Fig. S4.† The electrochemical performances of the treated electrodes were tested using galvanostatic cycling at room temperature with lithium metal as the counter electrode. In all the electrochemical tests, the potential range was set to 0.01–1.10 V (*versus* Li^+/Li). Fig. 5b displays the discharge/charge cycling behavior of the electrodes treated at 450 and 750 °C tested at a low current rate of 0.1 A g^{-1} for the first five cycles before shifting to the current of 0.5 A g^{-1} for 70 cycles. At 0.1 A g^{-1} , the electrodes treated at 450 and 750 °C delivered initial charges of 3128 and 2476 mA h g^{-1} , which correspond to a respective coulombic efficiency of 82% and 80%, respectively. After the second cycle, the coulombic efficiency rapidly increases up to $\sim 98\%$ and remains stable for 70 cycles. The capacity retention of the electrodes treated at 750 °C was found to be superior to that of the 450 °C treated electrodes, which demonstrates the importance of our designed layer of SiO_2 . In addition, we investigated the rate capability of Si electrodes treated at 450 and 750 °C at different current rates from 0.1 to 4 A g^{-1} as shown in Fig. 5c with corresponding galvanostatic charge/discharge profiles showing a capacity dependence on cycle numbers (Fig. S5†). Both electrodes have an excellent rate capability even at a high current rate of 4 A g^{-1} . They were cycled at a rate of 0.1 A g^{-1} for five cycles followed by measuring their rate capability at different current densities. The electrode treated at 450 °C displayed highly stable reversible capacities of about 3096, 2836, 2633 and 2270 mA h g^{-1} at current rates of 1, 2, 3 and 4 A g^{-1} , respectively. Moreover, a voltage plateau in the discharge/charge curves was also observed even at a high current density of 4 A g^{-1} , and then the electrode was able to recover back to 2723 mA h g^{-1} at a current density of 2 A g^{-1} . In contrast, the electrode treated at 750 °C also displayed a good rate capability but lower capacities due to our designed partial conversion of Si into SiO_2 .

This drastic stability and capacity difference between the 450 °C and 750 °C treated samples indicates the significance of the surface oxidation of Si into SiO_2 through the incorporation of an intimate layer of oxygen containing PVP. The decrease in the capacity of the 750 °C sample is most likely due to the previously mentioned oxidized Si (*i.e.* SiO_2). As shown in Fig. 5d, the impedance of the sample treated at 450 °C has a relatively higher charge transfer resistance (estimated from the diameter of the semicircle) than that of the sample treated at 750 °C which suggests that the difference in capacity is independent of the impedance of these cells. Since the 450 °C cell possessed a high impedance, this suggests that the difference in specific capacity is truly due to the transformation of Si into SiO_2 . Additionally, it is worth noting that the charge transfer resistance of the nontreated Si/PVP/PAN and the traditional SiNP (60%), PVDF (20%), and Super P (20%) electrodes without SHT was significantly higher than those of our modified electrodes and illustrates the main advantage of SHT on electrodes.

We also further compared the cycling behavior of the Si/PVP/PAN electrode treated at 450 and 750 °C to that of the SiNP/PVDF/Super P electrode as shown in Fig. 5e. The reference electrode SiNP/PVDF/Super P demonstrated a lithiation capacity

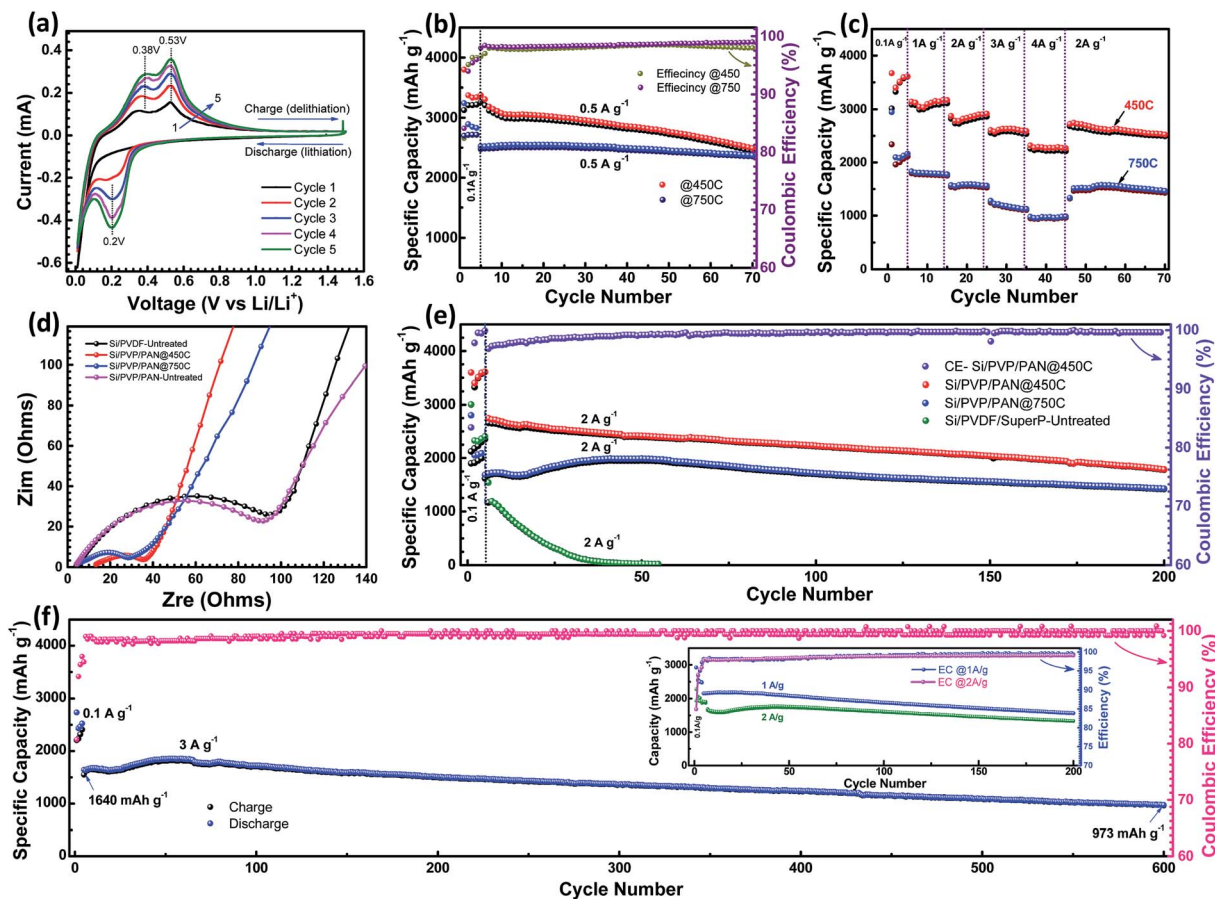


Fig. 5 Electrochemical characterizations of the Si electrodes: (a) CV curve for a coin cell treated at 750 °C and measured at a scan rate of 0.05 mV s^{-1} between 0.01 and 1.10 V (vs. Li^+/Li), (b) cycling stability of the electrodes treated at 450 and 750 °C at 0.1 A g^{-1} and 0.5 A g^{-1} , (c) rate capability of the electrodes treated at 450 and 750 °C, (d) Nyquist plots for the electrochemical impedance measurements after 50 cycles of Si/PVP/PAN treated at 450 and 750 °C, in comparison with non-treated Si/PVP/PAN and Si/PVDF/Super P electrodes, (e) cycling behavior of the Si/PVP/PAN treated at 450 and 750 °C at 0.1 A g^{-1} for the first five cycles and 2 A g^{-1} for the following cycles with Si/PVDF/Super P, and (f) long-term cycling stability of Si/PVP/PAN treated at 750 °C and cycled at 0.1 A g^{-1} for five cycles followed by 3 A g^{-1} for another 600 cycles, and the inset figure is for other electrodes treated at 750 °C and tested at 1 and 2 A g^{-1} .

of 3004 mA h g^{-1} in the initial cycle at 0.1 A g^{-1} and showed a poor cycling performance due to fast capacity decay to almost zero capacity at a current of 2 A g^{-1} (green line). This fast decay is associated with the fracturing of the Si layer caused by expansion of Si particles during repeated cycling. Although the electrode treated at 450 °C exhibits a better cycling performance than the reference electrode, it still shows a capacity loss from an initial reversible capacity of 2746 mA h g^{-1} fading to 1781 mA h g^{-1} at 2 A g^{-1} after 200 cycles with 99.8% of coulombic efficiency and with a capacity retention of 65%. Once again, the electrode treated at 750 °C exhibited excellent cycling stability at 2 A g^{-1} for 200 cycles after first five cycles at a low current rate of 0.1 A g^{-1} with a capacity retention of 85% while possessing a relatively lower capacity compared to the 450 °C sample. Both treated electrodes exhibited almost similar coulombic efficiency (99.8%) up to 200 cycles at a current of 2 A g^{-1} .

Furthermore, Fig. 5f shows the long-term cycling performance and coulombic efficiency of the other electrode treated at 750 °C and cycled at a high current rate of 3 A g^{-1} for 600 cycles

after an activation process at 0.1 A g^{-1} for five cycles. As observed, the treated Si electrode shows initial charge and discharge capacities of 2209 and 2736 mA h g^{-1} , respectively with a coulombic efficiency of 80% in the first cycle. This improvement of the lithium storage properties of the electrode treated at 750 °C is mainly related to the formation of the SiO_2 film on the Si particle surface. The SiO_2 film coating can provide a mechanically strong structural coating over the Si particles, while the lithium ions are still allowed to cross through during the lithiation processes. To further confirm the effect of PVP, the battery performance of the electrode without PVP was tested (ESI Fig. S6†). It is evident that without the incorporation of PVP, the Si/PAN electrode had a significantly poorer performance with severe cycle decay. This, in combination with the drastic differences in cycling performance between the 450 and 750 °C electrodes, provides strong evidence that the blend of PVP with PAN as a carbon precursor plays a crucial role in improving the electrochemical performance of the Si electrode. The charge/discharge cycle performance of battery cells with high silicon loading is presented in Fig. S7.† The result reveals

a high areal capacity of $\sim 3 \text{ mA h cm}^{-2}$ for the cell cycled at 0.5 A g^{-1} , and it is still maintained at around 1 mA h cm^{-2} at a higher rate of 6 A g^{-1} . The result indicates a promising avenue for high energy lithium ion batteries.

Fig. 6a and b show HAADF-STEM images with the corresponding EELS mapping for the Si, C, and O elements before and after 600 cycles, respectively. Before cycling, a clear concentration of O and C signals is found surrounding the Si particles. After cycling, the coating of O and C appeared to have disappeared which is to be expected after extended cycling. However, no aggregation of Si was found, and the scattered amorphized SiNPs are still hosted in the nitrogenized carbon framework. The SiNPs are still uniformly hosted in a cage of nitrogenated carbon after polymer carbonization. This suggests the strategy at which the electrode keeps cycling with minimal

loss in capacity. The EDS mapping after cycling of the same electrode treated at $750 \text{ }^\circ\text{C}$ is shown in ESI Fig. S8.† It is substantial to confirm that EELS and EDS mapping supply the elemental scale resolution to describe the distribution of elements everywhere in the electrode.

Conclusions

In summary, a high-performance Si anode was synthesized in this work by adopting a PVP/PAN polymer blend followed by a facile and economical slow heat treatment process. Different characteristics of the samples with and without PVP elucidated the interesting mechanism of the formation of the coatings on Si. The self-assembled PVP shell around the Si allowed for an amplified oxidation of Si, producing a robust SiO_2 shell while the decomposition of PAN introduced a nitrogen-rich carbon coating over the SiO_2 . When combined with a conductive graphene network, this material was able to deliver excellent cycling stability with a cycle retention of 60% over 600 cycles at a higher current density of 3 A g^{-1} as well as good rate capability.

Conflicts of interest

There are no conflicts to declare.

Acknowledgements

The authors would like to acknowledge the financial support by the Natural Sciences and Engineering Research Council of Canada (NSERC), the University of Waterloo and the Waterloo Institute for Nanotechnology. TEM and HAADF-STEM images were obtained at the Canadian Center for Electron Microscopy (CCEM) located at McMaster University. E.N.A. would like to thank the support of “Ministry of Higher Education and Scientific Research, Libya” for providing the scholarship.

References

- 1 M. Armand and J. M. Tarascon, *Nature*, 2008, **451**, 652–657.
- 2 M. Winter and R. J. Brodd, *Chem. Rev.*, 2004, **104**, 4245–4270.
- 3 J. M. Tarascon and M. Armand, *Nature*, 2001, **414**, 359–367.
- 4 R. Marom, S. F. Amalraj, N. Leifer, D. Jacob and D. Aurbach, *J. Mater. Chem.*, 2011, **21**, 9938–9954.
- 5 X. Su, Q. Wu, J. Li, X. Xiao, A. Lott, W. Lu, B. W. Sheldon and J. Wu, *Adv. Energy Mater.*, 2014, **4**, 1300882.
- 6 M. M. Thackeray, C. Wolverton and E. D. Isaacs, *Energy Environ. Sci.*, 2012, **5**, 7854–7863.
- 7 N.-S. Choi, Z. Chen, S. A. Freunberger, X. Ji, Y.-K. Sun, K. Amine, G. Yushin, L. F. Nazar, J. Cho and P. G. Bruce, *Angew. Chem., Int. Ed.*, 2012, **51**, 9994–10024.
- 8 T. B. Reddy and D. Linden, *Handbook of Batteries*, McGraw-Hill Education, 4th edn, 2011.
- 9 W.-J. Zhang, *J. Power Sources*, 2011, **196**, 13–24.
- 10 C. Zhang, F. Yang, D. Zhang, X. Zhang, C. Xue, Y. Zuo, C. Li, B. Cheng and Q. Wang, *RSC Adv.*, 2015, **5**, 15940–15943.

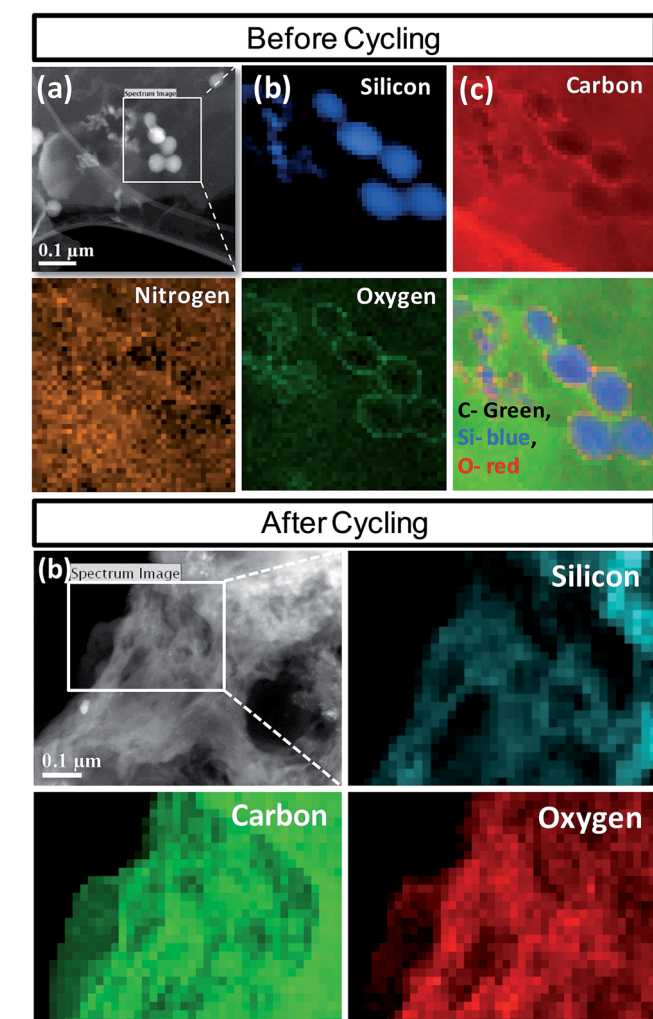


Fig. 6 Characterization of the electrode material before and after cycling for 600 cycles. (a) High-angle annular dark field scanning transmission electron micrograph (HAADF-STEM) of the electrode before cycling with the corresponding elemental mapping of Si, C, N, and O by EELS for the area marked in image (a), and (b) HAADF-STEM image of the electrode after cycling with the corresponding elemental (oxygen, carbon, and silicon) mapping by EELS for the area marked in the image (b).

- 11 F. M. Hassan, Q. Hu, J. Fu, R. Batmaz, J. Li, A. Yu, X. Xiao and Z. Chen, *ACS Appl. Mater. Interfaces*, 2017, **9**, 20603–20612.
- 12 C. K. Chan, H. Peng, G. Liu, K. McIlwrath, X. F. Zhang, R. A. Huggins and Y. Cui, *Nat. Nanotechnol.*, 2008, **3**, 31–35.
- 13 S. Y. Reece, J. A. Hamel, K. Sung, T. D. Jarvi, A. J. Esswein, J. J. H. Pijpers and D. G. Nocera, *Science*, 2011, **334**, 645–648.
- 14 H. Wu and Y. Cui, *Nano Today*, 2012, **7**, 414–429.
- 15 H. Li, Z. Wang, L. Chen and X. Huang, *Adv. Mater.*, 2009, **21**, 4593–4607.
- 16 J. R. Szczech and S. Jin, *Energy Environ. Sci.*, 2011, **4**, 56–72.
- 17 J. O. Besenhard, J. Yang and M. Winter, *J. Power Sources*, 1997, **68**, 87–90.
- 18 D. Aurbach, *J. Power Sources*, 2000, **89**, 206–218.
- 19 H. Kim, M. Seo, M.-H. Park and J. Cho, *Angew. Chem., Int. Ed.*, 2010, **49**, 2146–2149.
- 20 J. Yang, M. Winter and J. O. Besenhard, *Solid State Ionics*, 1996, **90**, 281–287.
- 21 M. Winter and J. O. Besenhard, *Electrochim. Acta*, 1999, **45**, 31–50.
- 22 C.-Y. Chou and G. S. Hwang, *J. Power Sources*, 2014, **263**, 252–258.
- 23 K. Feng, W. Ahn, G. Lui, H. W. Park, A. G. Kashkooli, G. Jiang, X. Wang, X. Xiao and Z. Chen, *Nano Energy*, 2016, **19**, 187–197.
- 24 F. M. Hassan, R. Batmaz, J. Li, X. Wang, X. Xiao, A. Yu and Z. Chen, *Nat. Commun.*, 2015, **6**, 8597.
- 25 S. H. Choi and Y. C. Kang, *ChemSusChem*, 2014, **7**, 523–528.
- 26 F. M. Hassan, V. Chabot, A. R. Elsayed, X. Xiao and Z. Chen, *Nano Lett.*, 2014, **14**, 277–283.
- 27 Y. Liu, Y. Liu, J.-H. Lee, C. Lee, M. Park and H.-Y. Kim, *Compos. Sci. Technol.*, 2015, **117**, 404–409.
- 28 K. Tang, Y. Li, H. Cao, C. Su, Z. Zhang and Y. Zhang, *Electrochim. Acta*, 2016, **190**, 678–688.
- 29 R. F. Ribeiro, L. C. Pardini, N. P. Alves and C. A. R. Brito Júnior, *Polimeros*, 2015, **25**, 523–530.
- 30 R. Devasia, C. P. R. Nair, P. Sivadasan, B. K. Katherine and K. N. Ninan, *J. Appl. Polym. Sci.*, 2003, **88**, 915–920.
- 31 H. Niu, J. Zhang, Z. Xie, X. Wang and T. Lin, *Carbon*, 2011, **49**, 2380–2388.
- 32 Y. T. Yeo, S. H. Goh and S. Y. Lee, *J. Macromol. Sci., Part A: Pure Appl. Chem.*, 1997, **34**, 597–603.
- 33 Q. Guo, J. Huang and X. Li, *Eur. Polym. J.*, 1996, **32**, 423–426.
- 34 Y. Jiang, D. Fang, G. Song, J. Nie, B. Chen and G. Ma, *New J. Chem.*, 2013, **37**, 2917–2924.
- 35 C. Li, C. Liu, W. Wang, J. Bell, Z. Mutlu, K. Ahmed, R. Ye, M. Ozkan and C. S. Ozkan, *Chem. Commun.*, 2016, **52**, 11398–11401.
- 36 G. D. Sorarù, S. Modena, P. Bettotti, G. Das, G. Mariotto and L. Pavesi, *Appl. Phys. Lett.*, 2003, **83**, 749–751.
- 37 L. Y. Yang, H. Z. Li, J. Liu, Z. Q. Sun, S. S. Tang and M. Lei, *Sci. Rep.*, 2015, **5**, 10908.
- 38 J. Li, D. Zhang, J.-b. Guo and J. Wei, *Chin. J. Chem. Phys.*, 2014, **27**, 718–724.
- 39 M. Beidaghi and C. Wang, *Adv. Funct. Mater.*, 2012, **22**, 4501–4510.
- 40 T. Hu, L. Chen, K. Yuan and Y. Chen, *Chem.–Eur. J.*, 2014, **20**, 17178–17184.
- 41 S. H. Choi, D. S. Jung, J. W. Choi and Y. C. Kang, *Chem.–Eur. J.*, 2015, **21**, 2076–2082.
- 42 S.-H. Kim, S.-H. Yook, A. G. Kannan, S. K. Kim, C. Park and D.-W. Kim, *Electrochim. Acta*, 2016, **209**, 278–284.
- 43 J. Yu, J. G. Shapter, J. S. Quinton, M. R. Johnston and D. A. Beattie, *Phys. Chem. Chem. Phys.*, 2007, **9**, 510–520.
- 44 M. Thakur, S. L. Sinsabaugh, M. J. Isaacson, M. S. Wong and S. L. Biswal, *Sci. Rep.*, 2012, **2**, 795.
- 45 J. S. Kim, D. Byun and J. K. Lee, *Curr. Appl. Phys.*, 2014, **14**, 596–602.
- 46 J. Yan, Q. Wang, T. Wei, L. Jiang, M. Zhang, X. Jing and Z. Fan, *ACS Nano*, 2014, **8**, 4720–4729.
- 47 S. Some, P. Bhunia, E. Hwang, K. Lee, Y. Yoon, S. Seo and H. Lee, *Chem.–Eur. J.*, 2012, **18**, 7665–7670.
- 48 S. Stankovich, D. A. Dikin, R. D. Piner, K. A. Kohlhaas, A. Kleinhammes, Y. Jia, Y. Wu, S. T. Nguyen and R. S. Ruoff, *Carbon*, 2007, **45**, 1558–1565.
- 49 Z. Xing, Z. Ju, Y. Zhao, J. Wan, Y. Zhu, Y. Qiang and Y. Qian, *Sci. Rep.*, 2016, **6**, 26146.
- 50 L. G. Bulusheva, M. A. Kanygin, V. E. Arkhipov, K. M. Popov, Y. V. Fedoseeva, D. A. Smirnov and A. V. Okotrub, *J. Phys. Chem. C*, 2017, **121**, 5108–5114.
- 51 M. Zhong, E. K. Kim, J. P. McGann, S.-E. Chun, J. F. Whitacre, M. Jaroniec, K. Matyjaszewski and T. Kowalewski, *J. Am. Chem. Soc.*, 2012, **134**, 14846–14857.
- 52 M. Ge, J. Rong, X. Fang and C. Zhou, *Nano Lett.*, 2012, **12**, 2318–2323.